University of Groningen

The extraordinary radio galaxy MRC B1221-423

Johnston, Helen M.; Broderick, Jess W.; Cotter, Garret; Morganti, Raffaella; Hunstead, Richard W.

IMPORTANT NOTE: You are advised to consult the publisher's version (publisher's PDF) if you wish to cite from it. Please check the document version below.

Document Version
Publisher's PDF, also known as Version of record

Link to publication in University of Groningen/UMCG research database

The extraordinary radio galaxy MRC B1221–423: probing deeper at radio and optical wavelengths

Helen M. Johnston,[1][*] Jess W. Broderick,[1,2] Garret Cotter,[3] Raffaella Morganti[4,5] and Richard W. Hunstead[1]

[1]*Sydney Institute for Astronomy, School of Physics, University of Sydney, NSW 2006, Australia*
[2]*School of Physics and Astronomy, University of Southampton, Southampton SO17 1BJ*
[3]*Department of Astrophysics, University of Oxford, Keble Road, Oxford OX1 3RH*
[4]*Netherlands Foundation for Research in Astronomy, Postbus 2, 7990 AA Dwingeloo, the Netherlands*
[5]*Kapteyn Astronomical Institute, University of Groningen, PO Box 800, 9700 AV Groningen, the Netherlands*

ABSTRACT

We present optical spectra and high-resolution multiwavelength radio observations of the compact steep-spectrum radio source MRC B1221−423 ($z = 0.1706$). MRC B1221−423 is a very young ($\sim 10^5$ yr), powerful radio source which is undergoing a tidal interaction with a companion galaxy . We find strong evidence of interaction between the active galactic nucleus (AGN) and its environment. The radio morphology is highly distorted, showing a dramatic interaction between the radio jet and the host galaxy, with the jet being turned almost back on itself. H I observations show strong absorption against the nucleus at an infall velocity of $\sim 250\,\mathrm{km\,s^{-1}}$ compared to the stellar velocity, as well as a second, broader component which may represent gas falling into the nucleus. Optical spectra show that star formation is taking place across the whole system. Broad optical emission lines in the nucleus show evidence of outflow. Our observations confirm that MRC B1221−423 is a young radio source in a gas-rich nuclear environment, and that there was a time delay of a few times 100 Myr between the onset of star formation and the triggering of the AGN.

Key words: galaxies: active – galaxies: interactions – galaxies: stellar content – radio continuum: galaxies.

1 INTRODUCTION

There is growing evidence of strong links between the triggering of powerful radio sources and gravitational interactions between galaxies. Many radio galaxies show signatures of tidal interactions, such as tails, bridges, shells and double nuclei (e.g. Heckman et al. 1986; Barnes & Hernquist 1992). These tidal encounters can lead to large increases in the amount of material being fed to the central black hole, thereby triggering the strong radio emission. The same tidal event that dumps gas in the vicinity of the nuclear black hole can produce a burst of star formation, and hence a population of young stars.

Further, the mechanical energy associated with relativistic radio jets can have a profound effect on the formation and evolution of galaxies, by heating the interstellar gas to the point where stars can no longer form. This *radio-mode feedback* has been suggested as the mechanism which suppresses star formation in massive galaxies; without such a feedback mechanism, galaxy evolution

models do not match the observed properties of galaxies (Croton et al. 2006).

So both starbursts and the growth of the nuclear black hole are intimately associated with the merger history of the galaxy. However, key questions remain unanswered. If mergers are responsible for the formation of both active galactic nuclei (AGN) and starbursts, why do we sometimes see one without the other? When we do see both, we usually see a young radio source together with an older starburst, suggesting that there is a delay between the starburst and the onset of AGN activity. What is the reason for this delay?

The compact steep-spectrum (CSS) sources are ideal laboratories for testing these connections. CSS sources are powerful but compact radio sources, with sizes of 1–20 kpc, so that the radio source lies well within its host galaxy. Their radio spectra are steep, $\alpha < -0.5$ ($S_\nu \propto \nu^\alpha$), peaking below 500 MHz. They have the same distribution in redshift as the rest of the powerful radio source population (see O'Dea 1998, for a review). The weight of evidence now is that CSS sources are small because they are young; if fuelling is sustained they are expected to evolve into classical large double-lobed radio sources (O'Dea 1998). All CSS sources accessible to detailed optical investigations show evidence for recent interactions
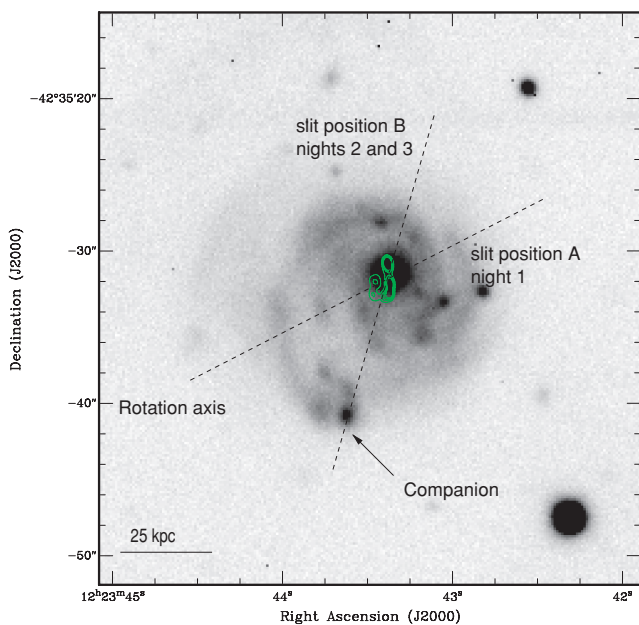
[*]E-mail: H.Johnston@physics.usyd.edu.au

and/or mergers, and evidence for young stellar populations and galaxy-wide starbursts have been found in many of these objects (see Holt 2009, for a review).

MRC B1221−423 is a member of a sample of southern radio sources similar in power to 3C sources (Burgess & Hunstead 2006a), with a radio power of $P_{1.4\,\mathrm{GHz}} = 1.8 \times 10^{26}\,\mathrm{W\,Hz^{-1}}$. The optical emission of the host galaxy is distorted, showing clear signatures of interaction, including tidal tails and shells (Safouris, Hunstead & Prouton 2003). Multicolour images show knotty blue star-forming regions, while the likely merging galaxy to the south is also significantly bluer than the host galaxy (Johnston et al. 2005, hereafter Paper I; see also Fig. 1). With a redshift of $z = 0.1706$ (Simpson et al. 1993), MRC B1221−423 is one of the nearest CSS sources; in the 3C sample, we need to go to $z = 0.3$ to find the first compact source as powerful as MRC B1221−423. The radio source has double lobes which lie well within the envelope of the host galaxy (Safouris et al. 2003). The age of the radio source, estimated from the power of the radio jets and total stored energy in the synchrotron plasma of the lobes (Rawlings & Saunders 1991), is only $\sim 10^5$ yr. As a young, nearby, bright CSS source, MRC B1221−423 is therefore an ideal candidate for testing the relationship between the AGN and its environment.

The goal of this study is to understand the relationship between the central AGN, which is the observational signpost of a growing black hole, and the environment of the galaxy. MRC B1221−423 provides a unique opportunity to measure both the age of the radio source and the star formation history of the galaxy, both of which are connected to the merger history of the galaxy.

In a previous paper (Paper I), we presented an analysis of multicolour *BVRIK* images of MRC B1221−423, which we used to analyse the change in stellar populations across the galaxy and its companion. We found evidence for three distinct stellar populations, with ages of about 15 Gyr, 300 Myr and less than 10 Myr. We concluded that the interaction with the companion galaxy triggered star formation in both galaxies, and after a substantial time delay, the infalling gas triggered activity in the central supermassive black hole.

In order to better understand the connection between the radio source and its environment, we have undertaken further radio and optical observations of MRC B1221−423, which we present in this paper. In Sections 2 and 3 we describe the radio images and H I absorption spectra of MRC B1221−423, and in Section 4 we describe the optical spectra. We have assumed a flat Λ cold dark matter (ΛCDM) cosmology with $H_0 = 71\,\mathrm{km\,s^{-1}\,Mpc^{-1}}$, $\Omega_\mathrm{M} = 0.27$ and $\Omega_\Lambda = 0.73$ throughout. At the distance of the galaxy, 1 arcsec corresponds to a distance of 2.876 kpc.

2 RADIO IMAGING

We observed MRC B1221−423 at 1344, 2282 and 18 880.5 + 19 648.5 MHz (20 cm, 13 cm and 12 mm wavebands) with the Australia Telescope Compact Array (ATCA), and also extracted unpublished, archival data at 1384 and 2496 MHz from the ATCA online archive[1]. Table 1 shows the details of these observations.

The data were reduced using standard procedures in MIRIAD (Sault, Teuben & Wright 1995). The effective bandwidth is either 104 MHz (13 channels, each of width 8 MHz) or 56 MHz (14 channels, each of width 4 MHz). However, at both 1384 and 2282 MHz, not all of the band is usable because the ATCA suffers from self-generated interference at integer multiples of 128 MHz. Hence, there is a slight shift of the effective frequency in both cases (see Table 1).

PKS B1934−638 was the primary calibrator at 20 and 13 cm, except for the observations from 2003 November where it was not observed. In this case, PKS B0823−500 as well as the 2280 MHz data from 2003 August were used to determine the flux density scale; we estimate that the uncertainty in this procedure is a few per cent at most. At 18.9 and 19.6 GHz, flux calibration was carried out using observations of Jupiter; we used the shortest baseline only, where Jupiter is not significantly resolved out.

The deconvolution and imaging procedure at each frequency consisted of a number of iterations of CLEAN plus self-calibration. Only after several rounds of phase-only self-calibration was a full amplitude and phase solution attempted. To ensure that the source model derived from the CLEAN components was as simple as possible (especially in the 12-mm waveband), natural weighting was used while self-calibrating. When it was clear that there was no further improvement in the image quality, both naturally and uniformly weighted images were created from the final self-calibrated visibilities. Table 1 contains a summary of the angular resolution and rms noise level in the vicinity of MRC B1221−423 in each total intensity image. The 18.9 and 19.6 GHz images were restored using the same beam size (that of the 18.9 GHz data) to allow these images to be averaged together for further analysis (average frequency 19 264.5 MHz). We estimate that the astrometry in the millimetre-wavelength images is accurate to ∼0.1 arcsec.

2.1 Morphology

At 8640 MHz, MRC B1221−423 is resolved into a north–south double structure with a projected separation of 4.3 kpc (1.5 arcsec),

Figure 1. *V*-band New Technology Telescope (ESO) image of the host galaxy (from Paper I), showing knotty features and tidal tails, strongly suggesting an ongoing interaction with the companion galaxy (arrowed). The 12 mm radio contours (Fig. 2) are overlaid to show the scale of the radio source in relation to the galaxy. The two slit positions (Table 3) are shown; spectrum A was taken along the rotation axis of the galaxy (see Section 4.1), while spectrum B was taken along the line joining the galaxy to its companion, which is close to the axis of the radio source.

[1]http://atoa.atnf.csiro.au

Table 1. Log of ATCA radio observations.

| Date (UT)	Array	Observing frequency (MHz)	Effective bandwidth (MHz)	Integration time (h)	Angular resolution[a] (arcsec × arcsec) N	U	Beam PA[b] N	U	rms noise[c] (mJy beam⁻¹) N	U
2004 Jan 9	6A	1344	104	8.44	14.05 × 9.58	8.12 × 5.71	−1°.1	−0°.3	0.45	0.55
1997 Jul 7	6A	1384	104[d]	0.06	13.48 × 10.02	10.12 × 6.60	−24°.3	−24°.8	1.2	1.4
2003 Aug 23	EW367	2282	56[e]	3.37						
2003 Nov 22	1.5D	2282	56[e]	6.18	14.19 × 13.64	4.20 × 3.31	16°.0	16°.4	0.42	0.55
1997 Jul 7	6A	2496	104	0.06	7.45 × 5.60	5.33 × 3.17	−24°.4	−23°.9	1.3	1.8
		18 880.5	104	7.59	1.09 × 0.67	0.57 × 0.34	9°.6	8°.0	0.11	0.18
2003 Jul 27	6D	19 648.5	104	7.59	1.09 × 0.67	0.57 × 0.34	9°.6	8°.0	0.11	0.18

[a]N – natural weighting; U – uniform weighting.
[b]Measured north through east.
[c]rms noise level in the vicinity of MRC B1221−423 in the total intensity image.
[d]One of the 8 MHz channels is flagged due to self-interference at 1408 MHz. The effective frequency is shifted slightly to 1382 MHz.
[e]One of the 4 MHz channels is flagged due to self-interference at 2304 MHz. The effective frequency is shifted slightly to 2280 MHz.
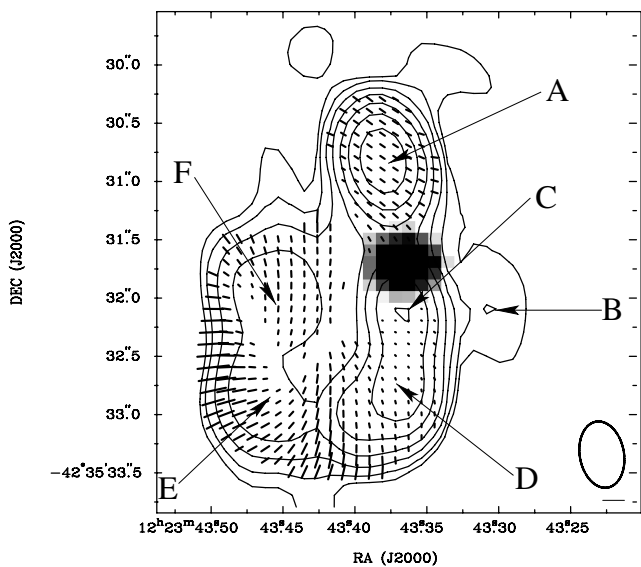

Figure 2. Total-intensity, uniformly weighted contour map of MRC B1221−423 at 19.3 GHz, with the position of the optical nucleus shown in grey-scale. The lowest contour is 0.75 mJy beam⁻¹, with each successive contour corresponding to a doubling of the surface brightness. Vectors show the projected electric field at each pixel location (not corrected for the Faraday rotation; pixel size 0.1 × 0.1 arcsec²); the scale bar in the bottom-right-hand corner corresponds to 50 per cent fractional linear polarization. An S/N cut-off of 5 in polarized intensity was used when plotting the polarization vectors. The various components have been labelled. The synthesized beam is shown in the bottom-right-hand corner.

as well as a third component to the east (Safouris et al. 2003). However, the finer angular resolution at 19.3 GHz reveals that MRC B1221−423 has a particularly striking radio morphology akin to a string of pearls (Fig. 2). The southern jet has undergone a dramatic interaction with the host galaxy, being bent through a full 180°. The projected length of the jet from the position of the optical nucleus to the peak of the furthest knot (knot F) is 8.6 kpc. On the other hand, the northern jet is much shorter: the projected separation is only 2.5 kpc.

2.2 Spectral energy distribution

Fig. 3 shows the spectral energy distribution (SED) of MRC B1221−423; the fluxes are tabulated in Table A1. Because the
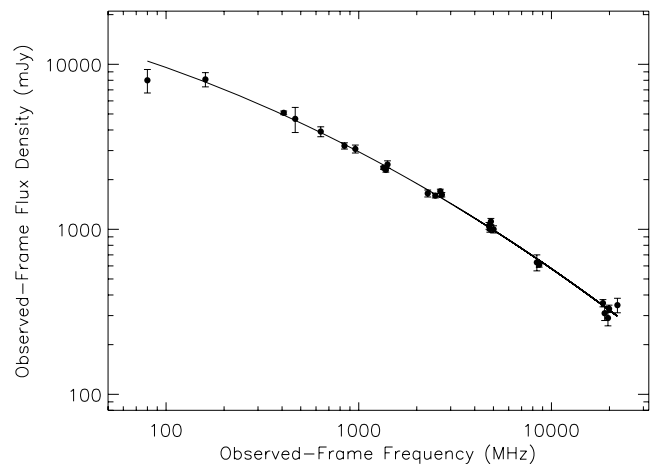
Figure 3. The observed-frame radio SED for MRC B1221−423, using all of the flux densities from Table A1. The 843, 4800 and 4850 MHz data points are the non-weighted averages of the two individual measurements at each of these frequencies. A second-order polynomial has been fitted to the SED: $\ln(S_\nu) = 10.15 - 0.01619 \ln(\nu) - 0.04295 [\ln(\nu)]^2$ with ν in MHz and S_ν in mJy. Though nearly all of the Parkes flux densities are affected by blending, the fit to the SED is not significantly altered if these data points are excluded from the fit (the two fits agree typically to within a few per cent).

source is only slightly extended at 20 and 13 cm, the 1344, 1382, 2280 and 2496 MHz flux densities were each determined by fitting an elliptical Gaussian with the MIRIAD task IMFIT. However, it was found that the most accurate way to measure the flux density at millimetre wavelengths was to sum the flux in a polygon that enclosed the source. The uncertainty for each of the new ATCA measurements is dominated by the internal calibration uncertainty. While the 20 and 13 cm flux densities are not affected by the weighting scheme used, we have quoted the 18.9 and 19.6 GHz flux densities from the naturally weighted images, which are approximately 3 per cent higher than the values from the uniformly weighted images. This will be due to some of the extended emission being resolved in the uniformly weighted images because of the finer resolution. However, the naturally weighted images themselves may be missing some extended flux, as, for example, can be seen by comparing our results with the ∼20 GHz flux densities reported by Ricci et al. (2006) and Murphy et al. (2010), which were derived using lower-resolution ATCA data than ours.

The observed-frame radio SED between 80 MHz and 22 GHz steepens with increasing frequency (Fig. 3). The spectral index α varies from -0.53 at 408 MHz to -0.88 at 22 GHz. Moreover, the 1.4 GHz luminosity is 1.8×10^{26} W Hz^{-1} for our assumed cosmological model. Further low-frequency measurements are needed to accurately determine the turnover frequency.

2.3 Linear polarization

Safouris et al. (2003) investigated the polarimetric properties of MRC B1221$-$423 at 4800 and 8640 MHz, finding that the fractional linear polarization m is as high as 35 per cent at 8640 MHz (resolution 1.4×0.63 arcsec^2). We now extend this analysis with our new ATCA high-frequency data. In Fig. 2, we have plotted polarization vectors at 19.3 GHz (resolution 0.57×0.34 arcsec^2). The vectors themselves were computed by first forming Stokes Q and U images at both 18.9 and 19.6 GHz from the self-calibrated visibilities; these images were restored with the same synthesized beam size. Averaged images were then produced for Stokes Q and U at 19.3 GHz, from which a total polarized intensity ($P = \sqrt{Q^2 + U^2}$) map, corrected for Ricean bias, was also formed. The average rms noise level in the 19.3 GHz Stokes Q and U images (σ_{QU}) in the vicinity of MRC B1221$-$423 is about 0.1 mJy beam^{-1}. Note that bandwidth depolarization is negligible for MRC B1221$-$423 in the 18.9 and 19.6 GHz bands.

High fractional linear polarization is also observed at millimetre wavelengths, particularly at the eastern edge of the source, where the mean fractional polarization is $\sim$50 per cent, with some pixels having $m \gtrsim 60$ per cent. The fractional polarization is also significant at the southern edge of the source (30–40 per cent), as well as between knots D and E ($\sim$25 per cent on average). Over the entire source, the median fractional polarization of the pixels is about 14 per cent. Further polarization statistics are shown in Table 2.

The orientation of the projected magnetic field with respect to the jet path varies significantly across the source. Knots A and C have similar polarization position angles even though there is a significant difference in the degree of polarization; in these regions the magnetic field is neither parallel nor perpendicular to the jet path. While the magnetic field becomes increasingly perpendicular to the jet path at knot D, it then becomes strikingly parallel to the jet between knots D and F where the extreme bending occurs. The magnetic field is also oriented circumferentially along the outer contours in this latter region, which was also observed in the lower-resolution 8640 MHz data (Safouris et al. 2003). In complete contrast, knot F exhibits magnetic fields that are closely perpendicular to the jet path.

Table 2. 19.3 GHz flux density, fractional polarization and polarization position angle measurements in the uniformly weighted image (Fig. 2). The measurements were made at the position of the peak pixel in Stokes I for each of the source components.

Component	S_I (mJy beam^{-1})	m (per cent)	χ ($\circ$)
A	89.9	13.0 ± 0.2	52.1 ± 0.3
B	1.5	$<20^a$	$\cdots$
C	48.4	1.9 ± 0.2	59 ± 3
D	42.0	5.7 ± 0.3	14.3 ± 1.2
E	11.8	14.7 ± 0.9	-67.0 ± 1.6
F	11.9	14.7 ± 0.9	-1.3 ± 1.6

^{a}3σ upper limit.

Note that after correcting for the Faraday rotation (see below), the intrinsic and observed polarization position angles are estimated to agree to within $\lesssim$5$\circ$ except for knot A, where the vectors need to be rotated anti-clockwise by $\sim$10$\circ$–15$\circ$.

2.4 Rotation measure synthesis

Faraday rotation measures (RMs) provide an important insight into the properties of the magnetoionic environment along the line of sight towards a radio source. Traditionally, the RM is determined from a linear fit between the polarization position angle χ and λ^2. However, this method suffers from several problems, such as position angle ambiguities. A superior Fourier-based technique, known as the Faraday RM synthesis, overcomes the problems associated with $\chi - \lambda^2$ fitting. Detailed descriptions of the method can be found in Brentjens & de Bruyn (2005) and Heald, Braun & Edmonds (2009). In brief, the complex linear polarization $P(\lambda^2) = Q(\lambda^2) + iU(\lambda^2)$ and complex Faraday dispersion function $F(\phi)$ are related via a relationship that is very similar to a Fourier transform. The Faraday depth ϕ, which is a more general quantity than the RM, is defined as

$$\phi = 0.812 \int_0^L n_e \boldsymbol{B} \cdot \mathrm{d}\boldsymbol{l} \tag{1}$$

where L is the path length through the magnetized plasma in pc, n_e is the thermal electron density in cm^{-3} and $\boldsymbol{B}$ is the magnetic field in μG. Measurements of P in a number of channels across one or more bandpasses can thus be used to form an 'RM data cube'; a slice through this cube at a particular spatial position gives a Faraday depth spectrum ($|F(\phi)|$ versus ϕ).

2.4.1 Low-frequency RM synthesis

First, we performed RM synthesis at 20 and 13 cm using three different approaches: 1344 MHz alone (13 $\times$ 8 MHz channels), 2280 MHz alone (13 $\times$ 4 MHz channels) and by combining the 1344 and 2280 MHz bands. There is no significant advantage in also including the 1382 and 2496 MHz observations because σ_{QU} is much higher than at 1344 and 2280 MHz ($\sim$0.12 and $\sim$0.20 mJy beam^{-1}, respectively, in the two latter cases). Each Stokes Q and U individual channel image was restored at the resolution of the 1344 MHz data (8.12 $\times$ 5.71 arcsec^2; PA $= -0\overset{\circ}{.}3$). Because MRC B1221$-$423 is only slightly extended at these frequencies, we formed Faraday depth spectra at the position of peak intensity in Stokes I. Though we cannot spatially resolve the individual components of the source, RM synthesis is still useful: the λ^2 coverage is greater than at higher frequencies, which reduces the uncertainty in the Faraday depth because the resolution in ϕ-space is much higher. Therefore, multiple Faraday depth components can potentially be resolved in ϕ-space even though we cannot spatially distinguish the different Faraday screens.

Inverse-variance weighting was applied to each channel when forming the Faraday depth spectra. A spectral index correction was also implemented (see Brentjens & de Bruyn 2005). The spectra were CLEANed to remove the sidelobes that are present due to incomplete λ^2 coverage; the response function is referred to as the rotation measure spread function (RMSF). A Gaussian 'restoring beam' was used when constructing each CLEANed spectrum (see Heald et al. 2009, for further details); the resolutions in ϕ-space are 591, 5123 and 74 rad m^{-2} full width at half-maximum (FWHM) at 1344 MHz alone, 2280 MHz alone and 1344 + 2280 MHz combined, respectively.
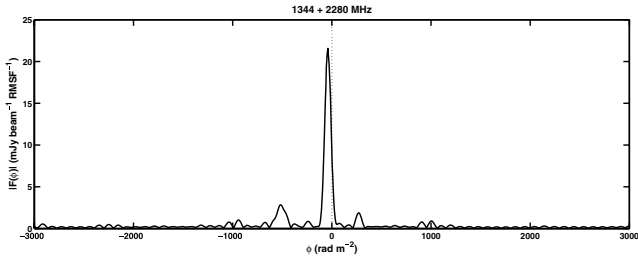
Figure 4. CLEANed 1344 + 2280 MHz Faraday depth spectrum for MRC B1221−423 at the position of peak intensity in Stokes *I*. The dotted line indicates a Faraday depth of zero. The Ricean bias has not been removed. The most prominent peak can be associated with the foreground Galactic RM.

Both the 1344 and 2280 MHz spectra are found to consist only of a single point-like Faraday depth component. However, the component shifts position between the two frequencies: the position of the peak is $-35 \pm 4 \, \mathrm{rad \, m^{-2}}$ at 1344 MHz, but $-220 \pm 30 \, \mathrm{rad \, m^{-2}}$ at 2280 MHz. The uncertainties take into account both the noise statistics and the estimated residual instrumental polarization. The components are bright enough such that the Ricean bias is not significant.

The shift in the position of the peak suggests that there is an unresolved distribution of components whose relative strengths vary with frequency. Indeed, multiple components are found when the 1344 and 2280 MHz data are combined to form a higher-resolution spectrum (Fig. 4). Apart from the bright peak at $-40 \pm 2 \, \mathrm{rad \, m^{-2}}$, there are weaker components above 10σ (about 1.3 mJy beam^{-1} RMSF^{-1}) at $+270$ and $-510 \, \mathrm{rad \, m^{-2}}$, the latter being extended over 1.6 beamwidths. However, these results must be interpreted with caution: the gap between the 20 and 13 cm bands introduces large sidelobes into the RMSF, which complicates the deconvolution process (though see the results at higher frequency below).

The Faraday depth of the brightest component in Fig. 4 is very similar to the mean RM of $-35 \, \mathrm{rad \, m^{-2}}$ calculated by Safouris et al. (2003) using the traditional linear fitting approach at 4800 + 8640 MHz. As discussed by Safouris et al. (2003), this result is consistent with the Galactic foreground RM in this region of the sky. We were also able to construct Faraday depth spectra at 1344 MHz for two nearby sources in the field: SUMSS J122328−423436 and SUMSS J122316−423922. Again, the derived Faraday depths are consistent with a Galactic magnetoionic screen being a significant, if not the main, source of the Faraday rotation.

2.4.2 High-frequency RM synthesis

We also attempted RM synthesis at higher frequencies by combining re-analysed 8640 MHz data (uniform weighting; resolution $1.14 \times 0.72 \, \mathrm{arcsec^2}$; PA $= -9°4$) with our millimetre-wavelength observations (naturally weighted but restored at the resolution of the 8640 MHz data); there are a total of 39 channels, each of width 8 MHz. Though the angular resolution is superior at these frequencies, the λ^2 coverage is poorer: the FWHM in ϕ-space is about $2600 \, \mathrm{rad \, m^{-2}}$ for inverse-variance weighting, and, like at 1344 + 2280 MHz, the RMSF contains large sidelobes because of the gaps between the bands. Because it is very easy for the peak of $|F(\phi)|$ to be shifted to the position of a nearby sidelobe for the lower signal-to-noise ratio (S/N) pixels, we only measured Faraday depths for the

pixels with peak polarized flux densities greater than 1 mJy beam^{-1} RMSF^{-1}, after applying a spectral index correction as above.

Fig. 5 shows a 3 cm + 12 mm Faraday depth map for MRC B1221−423. Each pixel has only one ϕ component (though the sidelobes significantly complicate the search for secondary components), and none of these components is extended. The Faraday depth varies from -1260 to $+330 \, \mathrm{rad \, m^{-2}}$, with a steep gradient from north to south: the mean Faraday depth for the top half of the source is $\sim -800 \, \mathrm{rad \, m^{-2}}$, while the mean for the bottom half is $\sim -30 \, \mathrm{rad \, m^{-2}}$. The latter value is close to the Galactic foreground RM (see above). The steep gradient in ϕ strongly suggests that the very large Faraday depths associated with the northern lobe are a consequence of a magnetoionic screen that is local to the source. The rest-frame Faraday depth will be a factor of $(1 + z)^2 = 1.37$ times higher than the observed-frame value after the Galactic contribution is removed from the latter. Assuming that the foreground Faraday depth is $\sim -40 \, \mathrm{rad \, m^{-2}}$, then the rest-frame Faraday depth at the position of peak intensity in Stokes *I* for the northern lobe is about $-1100 \, \mathrm{rad \, m^{-2}}$. From equation (1), large values of phi are a consequence of one or more of the following along the line of sight: (1) a dense medium, (2) a highly magnetized medium and (3) a long path length. The radio observations alone are not sufficient to disentangle the relative contributions.

To investigate further the magnetoionic environment of MRC B1221−423, we have also constructed a map of the depolarization ratio $m_{19264.5}/m_{8640}$ (Fig. 6). The northern lobe is significantly depolarized with decreasing frequency, implying small-scale inhomogeneities in the Faraday screen. This is likely to explain why there is not a prominent ϕ component at $\sim -1000 \, \mathrm{rad \, m^{-2}}$ in Fig. 4. On the other hand, the southern jet is not significantly depolarized
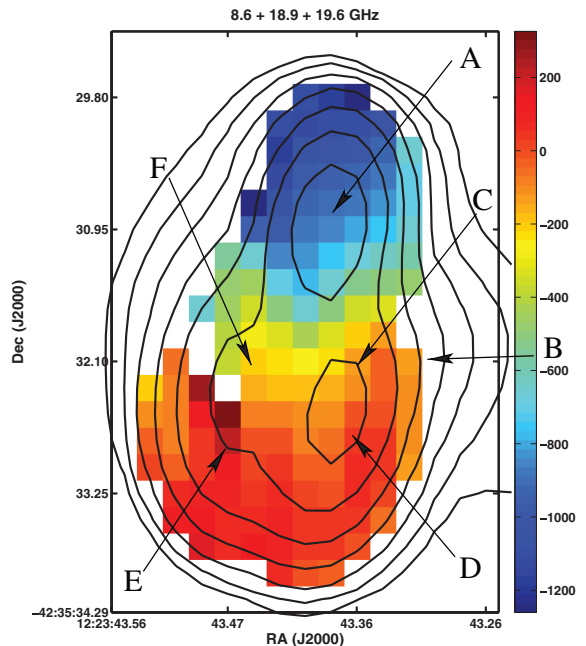
Figure 5. 8.6 + 18.9 + 19.6 GHz observed-frame Faraday depth map for MRC B1221−423 (angular resolution $1.14 \times 0.72 \, \mathrm{arcsec^2}$; beam PA $-9°4$; pixel size $0.23 \times 0.23 \, \mathrm{arcsec^2}$). The total-intensity radio contours are at 8640 MHz; the lowest contour is 2 mJy beam^{-1} and each successive contour corresponds to a doubling of the surface brightness. The colour bar has units of rad m^{-2}. The typical uncertainty in the Faraday depth for a given pixel is about 30 rad m^{-2}. The letters label the positions of the components seen in the 19.3 GHz map (Fig. 2).
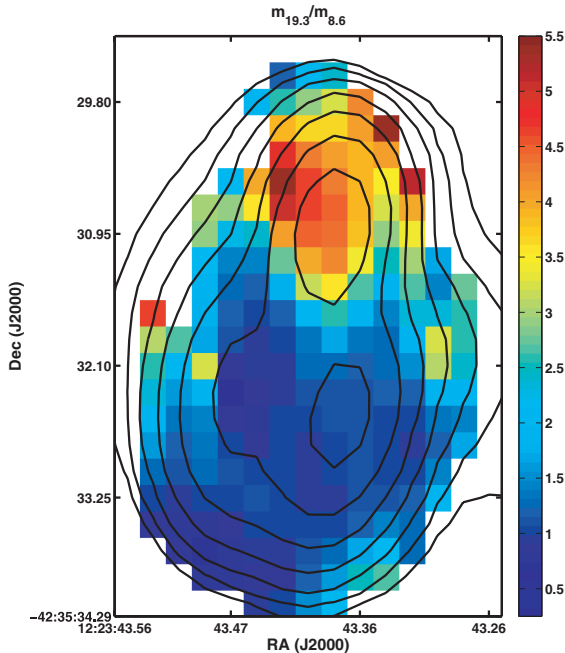
Figure 6. Depolarization ratio map between 8.6 and 19.3 GHz. The radio contour scheme is the same as in Fig. 5. An S/N cut-off of 5 in polarized intensity was used at both 8.6 and 19.3 GHz when constructing the map.

between 19264.5 and 8640 MHz; the fractional polarization in fact increases with decreasing frequency in some areas.

It is possible that we are seeing an orientation effect, with the radio source fore-shortened and the northern lobe seen through the galaxy. We discuss this possibility in Section 5.

3 RADIO SPECTROSCOPY

The H I observations of MRC B1221−423 were done with the ATCA for 2 × 12 hr on 2004 January 9 and 2004 July 17 using the 6-km array-configuration. All observations were done with 16 MHz bandwidth and a central frequency (for the first intermediate frequency (IF)) set to 1214 MHz. The first observation used 256 channels and two IFs while the second observation used 512 channels and only one IF.

We used PKS B1934−638 as bandpass and flux calibrator. To monitor the system gain and phase changes, PKS B1215−457 was observed as a secondary calibrator for 10 min every hour.

For the data reduction and visualization, we used the MIRIAD and KARMA (Gooch 1996) data reduction packages. For the line observations, after flagging and calibration, we separated the continuum from the line data in each individual data set by fitting either a first-order or a second-order polynomial to the line-free channels.

The continuum was subtracted using UVLIN by making a second-order fit to the line-free channels of each visibility record and subtracting this fit from the spectrum. After cleaning, Hanning smoothing was applied to each line cube. The final cube was derived by combining the data sets for the two observations. The beam size in the resulting uniformly weighted cube is 9.6 × 6.4 arcsec, PA = −1°. The rms noise in the Hanning cube is 0.77 mJy beam^{-1} per channel. Velocity resolution is 26 km s^{-1} after Hanning.

H I in absorption was clearly detected. The absorption, shown in Fig. 7, consists of a deep and relatively narrow component with a broad wing. The narrow component (FWHM ∼ 90 km s^{-1}) has a peak of −40.5 mJy centred on ∼51370 km s^{-1}. The optical depth
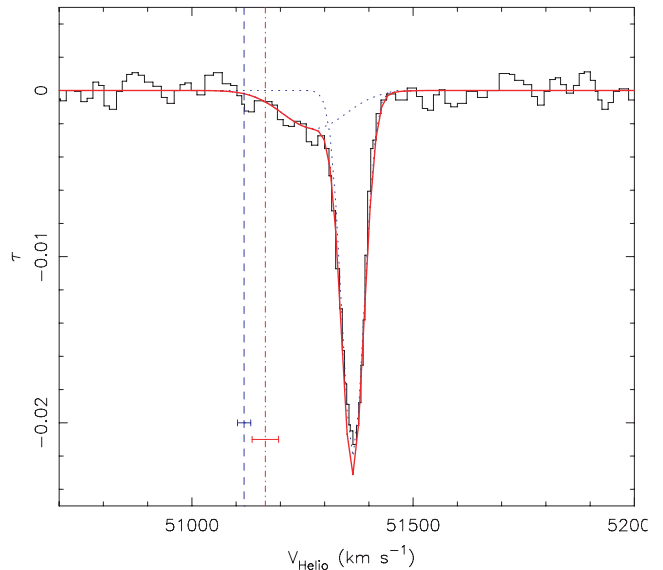
Figure 7. H I absorption against the nucleus of MRC B1221−423, showing large amounts of redshifted (infalling) material compared to the systemic velocity (dashed line). There is also a broad wing of absorption extending bluewards of the narrow absorption component. The thick red line shows the sum of two Gaussians fitted to the profile; the individual components are shown as the dotted blue lines. The vertical dashed line with error bar shows the stellar velocity ($cz = 51118 \pm 15$ km s^{-1}; see Section 4.2.3), while the vertical dash–dotted line shows the mean emission-line velocity ($cz = 51166 \pm 30$ km s^{-1}; see Section 4.3).

of this component is $\tau \sim 0.02$. Compared to the systemic velocity derived from the stars (51118 ± 15 km s^{-1}; see Section 4.2), this absorption component is redshifted by ∼250 km s^{-1}. The broad wing [estimated full-width at zero intensity (FWZI) ∼400 km s^{-1}] is blueshifted with respect to the narrow component by ∼150 km s^{-1}. It covers a velocity range extending to ∼51 100 km s^{-1}, therefore reaching velocities slightly blueshifted compared to the systemic velocity of the galaxy. The peak absorption of this wing has an optical depth of $\tau \sim 0.003$ (see Fig. 7).

No blueshifted component (which could be connected with outflowing gas) was detected to an optical depth limit of $\tau \sim 0.001$ (3σ). This is comparable with the optical depth detected in broad absorption components associated with outflows in other radio galaxies (Morganti, Tadhunter & Oosterloo 2005), so we would have been able to detect such outflows if they were present.

4 OPTICAL OBSERVATIONS

4.1 Observations and data reduction

Optical spectra were obtained on 2004 May 14–16 using the Double Beam Spectrograph on the ANU 2.3-m telescope at Siding Spring Observatory (Table 3). The detectors were two SITe 1752 × 532 CCDs with 15-μm pixels. For the first night, a dichroic filter with a cross-over wavelength of 6300 Å was used to split the light into the two arms of the spectrograph. Two gratings with 600 grooves mm^{-1} were used, giving a wavelength resolution of 2.2 Å over the wavelength range 4200–6120 Å in the blue and 6270–7130 Å in the red.

Safouris et al. (2003) used spectra taken at three different position angles to determine the angle of maximum gas rotation velocity; the (projected) axis of rotation was assumed to be perpendicular to this. The slit was oriented along this rotation axis, at a position angle of

Table 3. Journal of optical spectroscopic observations of MRC B1221−423. Two different set-ups were used, on the first night and remaining nights, respectively. The columns show the date of the observation, the wavelength range and the resolution, the exposure time, the position angle of the slit on the sky and the median seeing of the observations. The final column shows the slit position (Fig. 1).

UT date	λ range (Å)	FWHM (Å)	t_{exp} (ks)	PA (°)	Seeing (arcsec)	
2004 May 14	4200–6120	2.2	14.4	118	1.4	A
	6450–8000	2.2	12.6	118	1.4	
2004 May 15	3700–7500	4.3	23.4	−18	1.6	B
2004 May 16	3700–7500	4.3	23.4	−18	1.5	

118° (slit position A; Fig. 1). This set-up gave us high-resolution spectra with minimum rotational broadening of the line profiles.

For the remaining two nights, a plane mirror was used in place of the dichroic, so all light was sent to the blue arm of the spectrograph. A 300 grooves mm^{-1} grating gave us a wavelength resolution of 4.3 Å over the range 3700–7500 Å. The slit was oriented at a position angle of −18° so as to place both the galaxy and its interacting companion on the slit (slit position B; Fig. 1). This set-up gave us slightly lower wavelength resolution but continuous wavelength coverage of the blue region (rest-frame 3160–6400 Å), which is useful for age-dating stellar populations.

The spatial scale on the detector was 0.91 arcsec pixel^{-1}, corresponding to a linear scale of 2.6 kpc per pixel. On all three nights, a slitwidth of 1.5 arcsec was used, and pairs of 1800 s exposures were bracketed with NeAr arc-lamp exposures.

The IRAF software suite (Tody 1986) was used to remove the bias and pixel-to-pixel gain variations from each frame. Cosmic ray events were removed using the technique described by Croke (1995), as implemented in FIGARO (Shortridge 1993). The spectra were straightened in FIGARO so that the dispersion ran exactly along rows of the image, then a two-dimensional wavelength fit was performed to the arc images by fitting a third-order polynomial to the arc wavelengths as a function of pixel number, for each row of the image. These wavelength solutions were copied to the object images, interpolating between the bracketing arc exposures, and the data were rebinned so the wavelength–pixel relation was linear

and uniform across the image. The sky background was subtracted from each image by making a linear fit to the sky on either side of the galaxy, choosing regions well outside the wings of the galaxy profile. The spectra were corrected for atmospheric extinction, the telluric absorption features were removed by comparing with the spectrum of a smooth-spectrum standard taken at similar airmass and the spectra were flux-calibrated. We constructed two grand-sum spectra of the nucleus – one for each set-up (Table 3) – by aligning the individual spectra and summing, then correcting the summed spectrum for the Galactic reddening $A_V = 0.331$ mag (Schlegel, Finkbeiner & Davis 1998).

These spectra are shown in Fig. 8. They show narrow emission lines from ionized gas, on top of a continuum dominated by light from stars. In the following sections, we analyse these two components separately.

### 4.2 Stellar continuum

4.2.1 D4000 strength

The continua of many radio galaxies show UV excesses compared with normal elliptical galaxies. This excess may arise either from scattered nuclear light or from a population of young stars. In Fig. 9, we show the UV excess in MRC B1221−423, as measured by the strength of the 4000 Å break. We use $D'(4000)$ as defined by Tadhunter et al. (2002), which is the ratio of the flux between 4150 and 4250 Å (above the 4000 Å break) to the flux between 3750 and 3850 Å (below the break). This is a version of the original index $D(4000)$ proposed by Bruzual (1983), modified to exclude emission lines which are often present in the spectra of radio galaxies. Old stellar populations have large values of this index, while smaller values indicate a less pronounced 4000 Å break, and hence the presence of more UV light than expected from a passively evolving stellar population.

Fig. 9 shows that there is an excess of UV flux in all regions of MRC B1221−423 compared to a typical elliptical galaxy. Nowhere does the observed $D'(4000)$ approach the value of 2.3 typical for a passively evolving galaxy of solar metallicity (Tadhunter et al. 2005); the mean value over the galaxy (from the regions labelled G1 to G2) is 1.48 ± 0.05. Tadhunter et al. (2002) measured $D'(4000)$ for a sample of radio galaxies, and found values in the
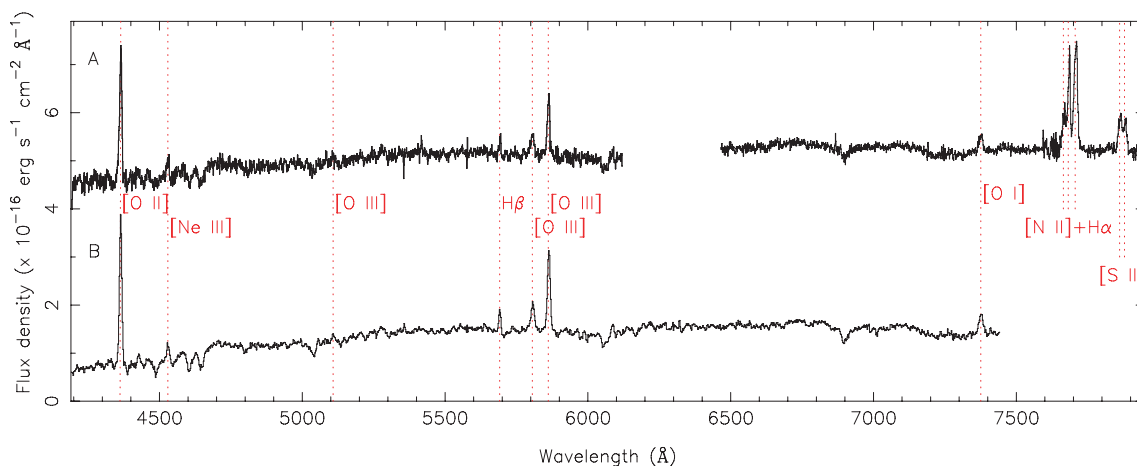
Figure 8. Spectrum of the nucleus of MRC B1221−423, extracted from the central 2.7 arcsec, with emission features identified. The top spectrum (spectrum A) is from the 2004 May 14 blue and red data, with the slit along the rotation axis of the galaxy; the bottom spectrum (spectrum B) is extracted from the combined data from 2004 May 15–16, with the slit along the line joining the galaxy to its companion. Spectrum A is offset in the y-direction by 4×10^{-16} erg s^{-1} cm^{-2} Å^{-1} for clarity.
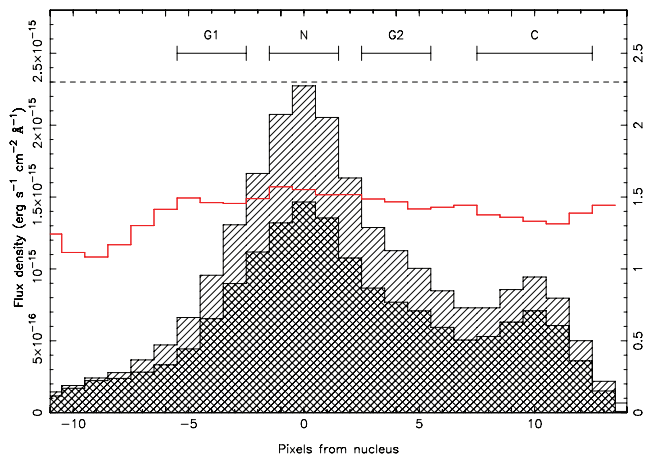
Figure 9. Spatial profiles of the flux along the slit in spectrum A in the rest wavelength ranges 3750–3850 Å (cross-hatching) and 4150–4250 Å (hatching). The ratio of the two, $D(4000)$, is shown as the solid line (right-hand scale); the dashed horizontal line shows $D(4000) = 2.3$, which is the value expected for a 12.5 Gyr elliptical galaxy of solar metallicity. Sub-solar metallicity ($Z = 0.4\,Z_\odot$) lowers this ratio to $D(4000) = 1.8$. The ratio measured for MRC B1221−423 is consistently below this, indicating the presence of a blue spectral component. The horizontal bars at the top of the plot indicated the regions extracted for the nuclear spectrum N, the companion galaxy C, and two regions away from the nucleus G1 and G2.

range ∼1.2–2.6. Tadhunter et al. (2005) found clear UV excesses in a sample of three powerful radio galaxies, and interpreted this as evidence of star formation associated with the radio source. The fact that we see a similar UV excess throughout MRC B1221−423 suggests that the star formation associated with the radio source is galaxy-wide.

4.2.2 Modelling the continuum

Next, we model the shape of the continuum SED in detail. The spectrum from 2004 May 14 (spectrum A) had different resolution, wavelength coverage and position angle to the grand-sum spectrum from the other two nights (spectrum B; Table 3), so we performed the following analysis for both summed spectra separately. We fitted three separate models to the continuum:

(i) a single-age stellar population, allowing the age to vary

(ii) an old stellar population plus a power-law continuum representing the AGN, with $F_\lambda \propto \lambda^\alpha$, allowing α to vary

(iii) an old stellar population plus a single-age young stellar population, allowing the age of the young stars to vary.

We used published isochrone spectral synthesis models from the GISSEL96 library (Bruzual & Charlot 1993) for the stellar populations. Both the 'old' and 'young' components were single-age stellar populations, representing instantaneous bursts of star formation. We used a Salpeter initial mass function with mass limits of 0.1 and $100\,M_\odot$ and solar metallicity, using the Gunn & Stryker (1983) stellar spectral atlas. For the old population, we used an instantaneous burst model with an age of 15 Gyr; the exact age of the 'old' population is not critical, since the spectrum changes little at these ages. For the young stellar population, we used instantaneous burst models with ages 10, 15, 20, 50, 80, 100, 150, . . . , 5000 Myr, giving us 14 models in total. We assembled the model spectra from the GISSEL96 library, and binned them to the same resolution as the observed spectra.

The spectra (observed and model) were binned into 20 Å bins, after which we removed bins corresponding to emission lines, residual night-sky lines, cosmic rays and atmospheric absorption bands. This resulted in 83 wavelength bins for spectrum A and 113 bins for spectrum B. We measure the flux in these bins for both our observed spectrum and models. The models were matched to the observed flux in a bin at (rest-frame) 4165 Å; the normalization was allowed to vary between 75 and 125 per cent of the flux of the observed spectrum, to allow for possible differences in slope between the model and the observed spectrum. Varying the fraction of the blue component, the normalization, and the power-law index or age of the young stars, the best-fitting model was found by calculating the χ^2 difference between the observed spectrum and each model spectrum. We assumed errors of ±4 per cent in each wavelength bin for the χ^2-fitting.

We began by fitting to the spectrum of the nucleus of the galaxy, extracting the central three rows (region N in Fig. 9), which correspond to the central 2.7 arcsec, or 7.8 kpc. The rest-frame wavelength range over which the fitting was done was 3600–6100 Å for spectrum A, and 3300–6100 Å for spectrum B. The results of this fitting are shown in Table 4. No single-age spectrum described the continuum well; the nominal best-fitting age of 2 Gyr systematically underestimates the flux in the red. Spectrum A was reasonably well

Table 4. Fits to the stellar continuum, in the nucleus and other regions of the galaxy. Fits are shown to spectrum A, taken along the rotation axis of the galaxy, and spectrum B, along the line joining the galaxy with its companion (lower resolution; Table 3). The three different models fitted to each spectrum are shown in column 2; column 3 shows the percentage of light at 4156 Å contributed by the blue component (where present); column 4 shows either the index of the power-law component or the age of the single-age stellar population component; column 5 shows the reduced χ^2 of the best fit. Ranges on the parameters indicate 1σ errors on the best fit. The lower half of the table shows the results of fits to the companion galaxy and to the main galaxy outside the nucleus.

Spectrum	Model	Per cent blue component	Parameter	χ^2_ν
Nucleus (A)	Single age	–	2.2–2.7 Gyr	4.18
	15 Gyr + power law	44 ± 5	$\alpha = -0.54 \pm 0.55$	2.14
	15 Gyr + young stars	42 ± 1	<23 Myr	1.35
Nucleus (B)	Single age	–	1.6–3 Gyr	2.10
	15 Gyr + power law	43 ± 5	$\alpha = 0.14 \pm 0.35$	3.51
	15 Gyr + young stars	43 ± 1	75–105 Myr	1.63
Companion (B)	15 Gyr + young stars	81 ± 3	150–200 Myr	0.86
Main galaxy (A)	'' ''	64 ± 4	<110 Myr	0.79
Main galaxy (B)	'' ''	64 ± 4	140–180 Myr	1.10
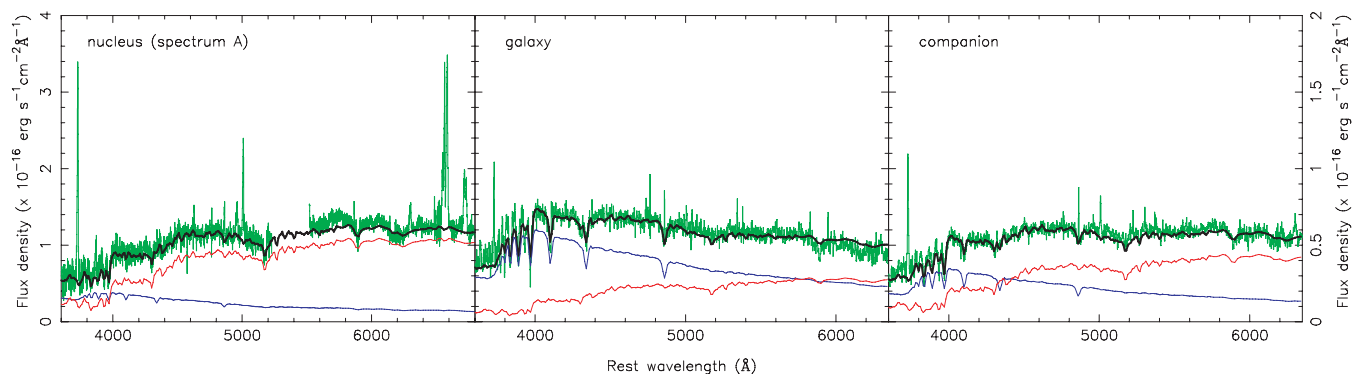
Figure 10. The best two-component model fits to the continuum of the nucleus, the galaxy outside the nucleus (G1, north of the nucleus) and the companion galaxy; the emission lines were not included in the fits. The apertures used to extract the spectra are shown in Fig. 9. Note that the *y*-scale of the left-hand panel is double that of the other two panels (right-hand scale). The parameters of the fits are shown in Table 4. The model spectrum (thick black line) is shown on top of the observed spectrum, together with the individual components, the old population (red) and the young population (blue).

modelled by the addition of a power law with $\alpha = -1$, though the same model did not fit spectrum B well. The addition of a population of young stars provided a much better fit to the spectrum. Both spectra A and B are well fitted by a model where ~43 per cent of the light at (rest-frame) 4200 Å is contributed by a young stellar population with an age of $\lesssim 100$ Myr. Spectrum A requires that the young population have an age of less than 23 Myr, while spectrum B was adequately fitted with models having ages between 75 and 105 Myr. The fit to spectrum A is shown in Fig. 10.

Thus, the continuum in the nuclear region is not well described by either a single-age population or a combination of old stars plus a power-law component. Instead, we require at least two stellar populations with different ages to reproduce the spectrum adequately.

We repeated this analysis with spectra extracted from other positions along the slit. We extracted the spectrum at the position of the companion galaxy; we also extracted regions of the main galaxy away from the nucleus (Fig. 10). The spectrum of the companion galaxy was extracted from spectrum B, including five rows centred 9 arcsec south from the nucleus (region C in Fig. 9). For slit position B, we could extract spectra from the southern and northern portions of the main galaxy separately. We extracted three rows (2.7 arcsec) beginning ±2.25 arcsec either side of the nucleus (regions G1 and G2 in Fig. 9) and fitted the two spectra separately; the results for both northern and southern spectra were consistent. For slit position A, the S/N of spectra extracted separately was insufficient, so we extracted the same regions but added the spectra together before fitting. As can be seen in Fig. 10, the spectrum of the galaxy outside the nucleus shows a much younger stellar population than the nucleus, with much stronger Balmer lines and a smaller 4000 Å break.

To quantify this, we again fitted the observed spectra with two single-age populations. The results of this fitting are shown in Table 4. The spectrum of the companion galaxy is well-described by a model where 80 per cent of the light is contributed by a 200 Myr old stellar population. The main galaxy away from the nucleus is best fitted with a slightly younger second population, with ages ~100 Myr. No significant difference was found between spectra obtained on either side of the nucleus.

We investigated including internal reddening as another free parameter; the fits to the nuclear spectra were marginally improved by the inclusion of 0.4 mag of extinction, but this did not significantly change the fitted ages of the underlying populations. The fit to the

companion galaxy also indicates a reddening of $A_V \sim 0.4$ mag, but the main galaxy outside the nucleus did not demand any reddening. These reddenings are significantly lower than the values we derived in Paper I, where we modelled the pixel colours using single-age populations.

This is broadly consistent with the results of Paper I, based on modelling of pixel colours, where we found an old population in the outskirts of the galaxy, an intermediate-age population ($\tau \sim 300$ Myr) in the companion and tidal tail, and a young population ($\tau \lesssim 10$ Myr) in the nucleus and blue 'knots'. Modelling the spectra enables us to best disentangle the contribution of the different populations, although our spatial resolution is not as good as in the images. Our fits to the pixel colours in the nucleus in Paper I were quite poor, indicating that our assumption of a single-age population was not a good one. The two-age fit to the spectrum in this work clearly gives a better description.

Thus we have found further evidence of starburst activity throughout the whole MRC B1221−423 system, with stars of different ages present in different regions. The youngest stars are in the nucleus, with slightly older populations in the companion galaxy and the main galaxy outside of the nucleus. The stellar models enable us to determine what fraction of the mass of the galaxy comes from each population. The mass fraction in young stars is not large: the young population in the nucleus with age $\lesssim 75$ Myr, which contributes nearly half the light at 4200 Å, contains less than 1 per cent of the mass. The highest mass fraction is found in the companion galaxy, where the 170 Myr population contributing 80 per cent of the light makes up 5 per cent of the mass of the galaxy.

4.2.3 Velocities

We determined the rotation curve of the stellar population by cross-correlating the spectrum extracted at different positions along the slit with a synthetic spectrum from Coelho et al. (2005). We extracted non-overlapping two-pixel spectra along the slit in spectrum A, the spectrum with the highest resolution, and cross-correlated with a synthetic spectrum of an F5V star (with $T_{\rm eff} = 6750$ K, $\log g = 4.5$), chosen as the best match to the continuum away from the nucleus of the galaxy. We cross-correlated the region from rest-frame 3845–4800 Å, chosen to avoid the bright emission lines, using the FIGARO routine SCROSS, which uses the method of Tonry & Davis (1979). The resulting stellar rotation curve is shown as the solid line in Fig. 12.

The redshift of the nucleus, which we take as the 'true' redshift of the galaxy, is 0.17053 ± 0.00005 ($cz = 51118 \pm 15$ km s^{-1}).

4.3 Emission-line gas

The spectrum of MRC B1221−423 shows numerous strong emission lines, characteristic of powerful radio sources. The emission lines enable us to probe the physical conditions and kinematics of the gas in the galaxy. Previous studies of CSS sources have found widespread evidence of outflows and disturbed kinematics in these systems (see e.g. Holt, Tadhunter & Morganti 2003; Emonts et al. 2006).

We subtracted the best fit to the continuum from each of spectrum A and spectrum B in order to model the emission lines. We used the fit comprising two single-age populations, as determined in Section 4.2.2 and Table 4.

Table 5 shows the measured parameters of the emission lines. The line centre and width (FWHM) were determined by fitting a Gaussian to the subtracted spectrum; the line flux was obtained by direct summation of the flux over a wavelength range four times the FWHM, except where such a width would also include neighbouring lines.

A combined fit to the emission lines of the blue spectrum A gives a heliocentric redshift of $z = 0.17068 \pm 0.00010$ ($cz = 51168 \pm 30$ km s^{-1}); the red spectrum gives $z = 0.17087 \pm 0.00013$ ($cz = 51225 \pm 40$ km s^{-1}). The emission lines in spectrum B give a redshift consistent with those in blue spectrum A: $z = 0.17067 \pm 0.00010$ ($cz = 51166 \pm 30$ km s^{-1}).

4.3.1 Kinematics of the emission lines

CSS sources often show broad, asymmetric emission lines in the nuclear region. We extracted the spectrum at the position of the nucleus by selecting the central two rows from each two-dimensional spectrum, corresponding to a linear size of 5.2 kpc. The brightest line, [O II] 3727, has a very asymmetric blue wing, as shown in Fig. 11. We modelled the line with two Gaussians, a narrow component (with width $\Delta v = 450$ km s^{-1} FWHM) at a velocity very similar to the rest-frame velocity, and a broad component ($\Delta v = 830$ km s^{-1} FWHM) blueshifted by 170 km s^{-1}. The velocity of this component is shown as the large red circle in Fig. 12.

The [O III] 4959, 5007 doublet also showed an asymmetric blue wing in the nuclear spectrum, though the broad component was noticeably weaker, compared to the narrow component, than in the [O II] 3727 line. We fitted two Gaussian components to each line, constraining the wavelength ratio to the known value and the flux ratios to be 3.0:1, given by the transition probabilities; we also constrained the corresponding components (broad and narrow) to have the same linewidth in each line of the doublet. The widths of

Table 5. Emission-line measurements, from the rest-frame spectrum B with the model stellar continuum subtracted.

Line	Flux ($\times 10^{-16}$ erg s^{-1} cm^{-2})	FWHM (km s^{-1})
[O II] 3727	37.0 ± 1.5	660 ± 40
[Ne III] 3869	5.0 ± 0.6	730 ± 70
He II 4686	<0.12	–
Hβ 4861	6.1 ± 0.4	470 ± 40
[O III] 4959	8.6 ± 0.2	600 ± 30
[O III] 5007	22.2 ± 0.2	600 ± 30
[O I] 6300	7.0 ± 0.4	680 ± 30
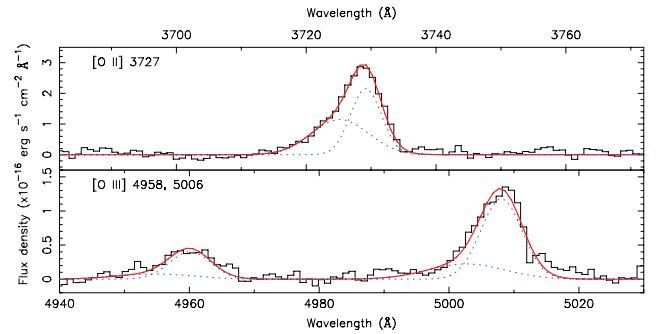
Figure 11. Line profile fitted to the [O II] and [O III] lines extracted from the central two rows of spectrum A. The dotted lines show the two separate Gaussian components which were fitted. The line separations and strengths of the [O III] doublet were constrained to those known from atomic physics, and we required the separation of the broad and narrow components to be the same as for the [O II] line.
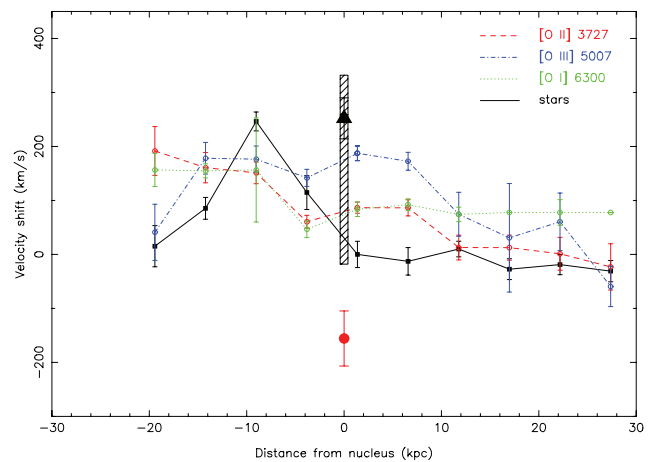

Figure 12. Rest-frame velocity profiles along spectrum A, for the stellar continuum (solid line) and three emission lines: [O II] 3727, [O III] 4959, 5007 and [O I] 6300. The positive direction is to the south-east. Velocity zero is taken as the velocity of the absorption-line component at the position of the nucleus (corrected to the heliocentric frame, see Section 4.2.3). The large filled triangle shows the velocity of the narrow H I absorption component (Section 3), while the large filled circle shows the velocity of the broad [O II] emission. The hatched bar shows the full width (FWZI) of the H I absorption.

the Gaussians were consistent with the linewidths from the fit to the [O II] line, so we constrained them to be the same, allowing only the line intensities to vary. The resulting fit was also acceptable, though with a much weaker broad component. None of the other emission lines – Hβ, [Ne III], [O I] – showed any evidence for the presence of a broad component, so if present it must be extremely weak.

To investigate the gas kinematics away from the nucleus, we extracted spectra from different positions along the slit, as described in Section 4.2.3. Except for the nuclear spectrum, there was no evidence for a broad component, so we fitted a single Gaussian to each line. The resulting velocity profiles are shown in Fig. 12.

4.3.2 Ionization state

The ionization state of the MRC B1221−423 is quite low; [O II] 3727 is stronger than [O III] 5007, while He II 4686 is extremely weak. The line-ratios are characteristic of 'low ionization nuclear emission-line regions' or LINERs (Heckman 1980). The
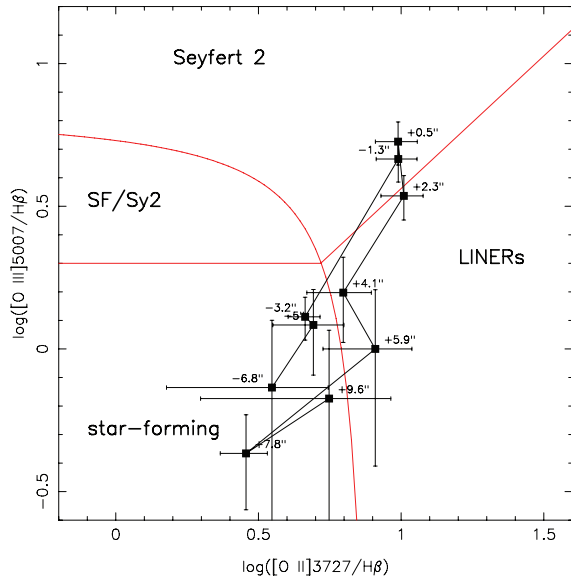
Figure 13. Ionization mechanism diagnostic plot using the line-ratios [O II]3727/Hβ and [O III]5007/Hβ. Data points represent the observed spectra extracted in non-overlapping two-pixel steps along the slit in spectrum A. The red lines show the classification regions from Lamareille (2010). The emission lines are AGN-like close to the core, and become more star formation like further out.

temperature-sensitive [O III] line intensity ratio (λ5007+λ4959)/λ4363 is relatively low, indicative of high temperatures and/or densities.

The Hα to Hβ ratio is extreme; we measure $F_{H\alpha}/F_{H\beta} = 6.36$, much larger than the case B recombination value of 2.86 (e.g. Osterbrock 1989). If this were due to reddening, it would imply $A_V = 2.3$ mag, which is much higher than the value we derived from the stellar continuum, $A_V \sim 0.4$ mag (Section 4.2.2). Interestingly, this is similar to our earlier estimate of the reddening in the nucleus from modelling the SEDs (Paper I), where we found $A_V = 1.9$ mag. If the Balmer emission is mainly from the nucleus, we could be seeing the effect of very localized dust. On the other hand, this ratio could be being distorted by the presence of Hβ in absorption; for comparison, we measure $F_{H\gamma}/F_{H\beta} = 0.48$, compared to an expected value of 0.47 for $T = 10^4$ K. Large ratios of Hα/Hβ are seen in many LINER sources (Heckman 1980).

We can investigate the changing ionization state of the gas by comparing emission-line intensity ratios at different positions along the slit (Baldwin, Phillips & Terlevich 1981). In Fig. 13, we show the diagnostic diagram for the line-ratios [O II]3727/Hβ and [O III]5007/Hβ, using the Gaussian fits to the lines described in Section 4.3.1. We also show the classification regions of Lamareille (2010). The diagram clearly shows the changing ionization state at different distances from the nucleus. Close to the nucleus the line-ratios are consistent with ionization by the AGN, while at larger distances the line-ratios look more like star-forming galaxies.

5 DISCUSSION AND CONCLUSIONS

We have presented detailed radio and optical spectroscopic observations of MRC B1221−423, a young CSS source which is currently undergoing a merger. Our main findings are:

(i) a highly distorted radio morphology
(ii) a large Faraday depth and significant depolarization in the northern, less distorted, lobe of the source

(iii) the presence of redshifted H I in absorption
(iv) a range of stellar ages in the galaxy
(v) strong emission lines with relatively low ionization.

The radio observations of MRC B1221−423 show dramatic interaction between the southern radio jet and the host galaxy, together with infalling gas. This jet appears to be bent through a full 180°. The alignment of the magnetic field along the jet supports the interpretation of the feature as a single connected structure, with the magnetic field being oriented circumferentially where the extreme bending occurs. This is suggestive of a strong interaction with high-density material. Interestingly, the RM synthesis shows no evidence of a dense interstellar medium (ISM) where the jet bends.

The much shorter extent of the radio emission to the north, as well as the steep gradient in Faraday depth from north to south, suggests the presence of a dense and possibly highly magnetized medium local to the source. One possibility is that we could be seeing an orientation effect, with the northern jet pointed away from us and seen behind the galaxy. Large changes of jet direction in radio galaxies have been modelled as the result of a helical jet (see e.g. Hunstead et al. 1984; Conway & Murphy 1993); it is possible that a helix viewed almost head-on could explain the extreme change in projected jet direction that we see in MRC B1221−423. The lack of evidence for a dense ISM at the bend of the jet from the RM synthesis would be consistent with this interpretation. Alternately, the infalling gas could be interacting with the jet, producing both the change in jet direction and the different polarization in the lobes. Saikia & Gupta (2003) found a high degree of polarization asymmetry in CSS sources, which they ascribed to interaction of the jets with infalling material.

H I was clearly detected in absorption, with a narrow component at a velocity of +250 km s^{-1} compared to the velocity of the galaxy determined from the stellar component. Both this absorption and the radio continuum observations suggest the source is in a gas-rich environment. There is also a broader wing of H I absorption extending to the systemic velocity. The velocity shift with respect to the stellar redshift suggests large amounts of infalling gas. It should be noted, however, that the velocities of the H I, particularly of the broad component, are quite similar to the range of velocities shown by the emission lines (see Fig. 12), so it is possible that the H I absorption is just part of the overall distribution of gas. Redshifted H I absorption is not common in similar sources: of 14 sources studied by Holt, Tadhunter & Morganti (2008), most showed significantly *blueshifted* H I absorption, reflecting outflow. Only two of their sources — PKS B0023−263 and PKS B1934−638 — showed redshifted H I absorption.

The location of the absorbing gas is not clear. A comparison can be drawn with the radio galaxy NGC 315, which shows two absorption systems against the central region (Morganti et al. 2009). In addition to the redshifted narrow component ($v \sim +490$ km s^{-1}), NGC 315 has a broader (FWZI $\sim$150 km s^{-1}) component redshifted by $\sim$80 km s^{-1} compared to the systemic velocity. Morganti et al. (2009) concluded from velocity gradients seen in *VLBI* data that the broad component arises from gas falling into the nucleus, while the narrow component arises from more distant gas clouds falling towards the galaxy. By analogy, we might be seeing a similar situation in MRC B1221−423. The narrow absorption component could represent a discrete cloud at some distance from the galaxy, while the broad absorption arises much closer to the nucleus, either from a circumnuclear torus or from the infalling gas that is fuelling the nuclear activity. Higher resolution H I observations are needed to distinguish these possibilities.

Optical spectra of MRC B1221−423 reveal disturbed kinematics. Most of the ionized gas is at velocities similar to that of the stars, but in the nucleus we detect a broad blueshifted component to the emission lines with $\Delta v = 830 \ \mathrm{km \, s^{-1}}$ FWHM, which we interpret as evidence for outflow of emission-line gas in the nucleus. Since it is only visible in the nucleus, this could arise from gas interacting with the radio jet: the fact that it is blueshifted might support the interpretation that the jet axis is strongly inclined to the line of sight.

The ionization state of the gas is relatively low, with [O II] 3727 stronger than [O III] 5007, and a very weak He II 4686 line. The line-ratios change as a function of position, with the emission being dominated by the AGN close to the nucleus, and becoming more star formation like further out. A similar result was found in the sample of compact radio sources studied by Holt, Tadhunter & Morganti (2009), where the ionization in the nuclear regions is dominated by the central AGN. Like them, we find a lower [O III] 5007 luminosity than extended sources with similar radio luminosity in their comparison sample.

Star formation activity is evident over the whole system, including the companion galaxy. The youngest stellar population is close to the nucleus, consistent with the idea that the same inflows of gas that have triggered star formation are also triggering the activity of the central black hole.

Our previous work on MRC B1221−423 suggested the following scenario: tidal interaction with the companion galaxy triggered different phases of star formation in the two galaxies, and then, after a substantial delay, the central AGN was triggered to produce the radio emission. The current observations support this model. We have found evidence of past episodes of star formation, probable evidence for infalling gas and indication of interaction between the radio jet and its environment.

Our work confirms the fact that young, powerful radio sources tend to live in a gas-rich nuclear environment. Further, we show that the AGN is younger than the starburst. The ages of the stellar populations are comparable with the orbital period of the companion, which we estimate to be $\sim 10^8$ yr, based on the projected separation of the companion galaxy from the nucleus, together with an estimate of the mass of the galaxy from the K-band luminosity. The faint arcs to the north-east (Safouris et al. 2003) suggest there have been previous tidal interactions. These time-scales suggest a time delay of $\sim$a few times 100 Myr between the tidal event (that triggered star formation) and the onset of AGN activity. Such delays have been found in several nearby AGN (see e.g. Tadhunter, Dickson & Shaw 1996; Emonts et al. 2006; Davies et al. 2007), but this is possibly one of the best examples. In recent work, Wild, Heckman & Charlot (2010) constructed a sample of starburst galaxies from the Sloan Digital Sky Survey. They found that the rate of accretion on to the central black hole, as measured by the strength of the [O III] line, rises steeply about 250 Myr after the onset of star formation. They speculate that the accretion on to the black hole may be regulated by the starburst, with the accretion being dominated by low-velocity stellar winds, and accretion at early times being suppressed by supernovae.

We have also found indication of a possible infall of cold gas that could provide the fuel for the AGN. We note that the age distribution of the stellar populations is consistent with a picture in which cold or cooling gas is driven by the merger towards the centre of the host galaxy to fuel the AGN from relatively large radii, and that this gas begins to form stars while it is still well away from the nucleus. This contrasts with the situation in lower-luminosity radio sources in cluster environments, which, even though they sometimes contain the most massive black holes, are accreting in an environment dominated by hot gas and are associated with an accretion mode that produces low-power radio jets.

REFERENCES

Baldwin J. A., Phillips M. M., Terlevich R., 1981, PASP, 93, 5
Barnes J. E., Hernquist L., 1992, ARA&A, 30, 705
Bolton J. G., Shimmins A. J., 1973, Aust. J. Phys. Astrn. Supp., 30, 1
Brentjens M. A., de Bruyn A. G., 2005, A&A, 441, 1217
Bruzual G., 1983, ApJ, 273, 105
Bruzual G., Charlot S., 1993, ApJ, 405, 538
Burgess A. M., Hunstead R. W., 2006a, AJ, 131, 100
Burgess A. M., Hunstead R. W., 2006b, AJ, 131, 114
Coelho P., Barbuy B., Meléndez J., Schiavon R. P., Castilho B. V., 2005, A&A, 443, 735
Conway J. E., Murphy D. W., 1993, ApJ, 411, 89
Croke B. F. W., 1995, PASP, 107, 1255
Croton D. J. et al., 2006, MNRAS, 365, 11
Davies R. I., Sánchez F. M., Genzel R., Tacconi L. J., Hicks E. K. S., Friedrich S., Sternberg A., 2007, ApJ, 671, 1388
Duncan R. A., Sproats L. N., 1992, PASA, 10, 16
Emonts B. H. C., Morganti R., Tadhunter C. N., Holt J., Oosterloo T. A., van der Hulst J. M., Wills K. A., 2006, A&A, 454, 125
Gooch R., 1996, in Jacoby G. H., Barnes J., eds, ASP Conf. Ser. Vol. 101, Astronomical Data Analysis Software and Systems V, Astron. Soc. Pac., San Francisco, p. 80
Gregory P. C., Vavasour J. D., Scott W. K., Condon J. J., 1994, ApJS, 90, 173
Gunn J. E., Stryker L. L., 1983, ApJS, 52, 121
Heald G., Braun R., Edmonds R., 2009, A&A, 503, 409
Heckman T. M., 1980, A&A, 87, 152
Heckman T. M., Smith E. P., Baum S. A., van Breugel W. J. M., Miley G. K., Illingworth G. D., Bothun G. D., Balick B., 1986, ApJ, 311, 526
Holt J., 2009, AN, 330, 226
Holt J., Tadhunter C. N., Morganti R., 2003, MNRAS, 342, 227
Holt J., Tadhunter C. N., Morganti R., 2008, MNRAS, 387, 639
Holt J., Tadhunter C. N., Morganti R., 2009, MNRAS, 400, 589
Hunstead R. W., Murdoch H. S., Condon J. J., Phillips M. M., 1984, MNRAS, 207, 55
Johnston H. M., Hunstead R. W., Cotter G., Sadler E. M., 2005, MNRAS, 356, 515 (Paper I)
Lamareille F., 2010, A&A, 509, A53
Large M. I., Mills B. Y., Little A. G., Crawford D. F., Sutton J. M., 1981, MNRAS, 194, 693
Mauch T., Murphy T., Buttery H. J., Curran J., Hunstead R. W., Piestrzynski B., Robertson J. G., Sadler E. M., 2003, MNRAS, 342, 1117
Morganti R., Tadhunter C. N., Oosterloo T. A., 2005, A&A, 444, L9
Morganti R., Peck A. B., Oosterloo T. A., van Moorsel G., Capetti A., Fanti R., Parma P., de Ruiter H. R., 2009, A&A, 505, 559
Murphy T., Mauch T., Green A., Hunstead R. W., Piestrzynska B., Kels A. P., Sztajer P., 2007, MNRAS, 382, 382
Murphy T., Sadler E. M., Ekers R. D., Massardi M. et al., 2010, MNRAS, 402, 2403

Table A1. B1221−423 radio flux densities.

Frequency (MHz)	S_ν (mJy)	Survey/ telescope	Reference
80	8000 ± 1300^a	CCA	Slee & Higgins (1973), Slee (1995)
160	8100 ± 800^a	CCA	Slee (1977, 1995)
408	5080 ± 130	MRC	Large et al. (1981)
468	4670 ± 810	PKS	Wills (1975)
635	3910 ± 270	PKS	Wills (1975)
843	3300 ± 200	MOST	Burgess & Hunstead (2006a)
843	3110 ± 90	SUMSS	Mauch et al. (2003), Murphy et al. (2007)
960	3070 ± 170	PKS	Wills (1975)
1344	2360 ± 50	ATCA	This paper
1382	2290 ± 70	ATCA	This paper
1410	2470 ± 130	PKS	Wills (1975)
2280	1650 ± 80	ATCA	This paper
2496	1600 ± 50	ATCA	This paper
2650	1700 ± 50	PKS	Wills (1975)
2700	1620 ± 50	PKS	Bolton & Shimmins (1973)
4740	1050 ± 50^b	ATCA	Burgess & Hunstead (2006b)
4790	1010 ± 50^{bc}	ATCA	Duncan & Sproats (1992)
4800	1010 ± 20	ATCA	Safouris et al. (2003)
4800	999 ± 41	ATCA	Murphy et al. (2010)
4850	1090 ± 60^d	PMN	Wright et al. (1994)
4850	1140 ± 60	PMNM	Gregory et al. (1994)
5009	1000 ± 50	PKS	Wills (1975)
8400	630 ± 70	PKS	Wright et al. (1990), Wright & Otrupcek (1990)
8640	610 ± 20	ATCA	Safouris et al. (2003)
18 500	357 ± 18	ATCA	Ricci et al. (2006)
18 880.5	310 ± 30	ATCA	This paper
19 648.5	290 ± 30	ATCA	This paper
19 904	330 ± 17	AT20G	Murphy et al. (2010)
22 000	347 ± 35	ATCA	Ricci et al. (2006)

Notes. CCA – Culgoora Circular Array; MRC – Molonglo Reference Catalogue; MOST – Molonglo Observatory Synthesis Telescope; SUMSS – Sydney University Molonglo Sky Survey; PKS – Parkes Catalogue; ATCA – Australia Telescope Compact Array; PMN – Parkes-MIT-NRAO Survey; PMNM – PMN Map Catalogue; AT20G – Australia Telescope 20 GHz Survey.
^{a}Flux density uncertainty calculated using the error analysis from the original CCA catalogue, but not including the original uncertainty associated with the flux density scale; the scale was refined by Slee & Siegman (1988).
^{b}Flux density uncertainty not stated in the reference; a ± 5 per cent uncertainty has been assumed.
^{c}The original measurement has been rescaled so that it is consistent with the current ATCA flux density scale.
^{d}General-width fit; the fixed-width fit has a similar flux density (1100 ± 60 mJy).

O'Dea C. P., 1998, PASP, 110, 493

Osterbrock D. E., 1989, Astrophysics of Gaseous Nebulae and Active Galactic Nuclei. University Science Books, Mill Valley

Rawlings S., Saunders R., 1991, Nat, 349, 138

Ricci R., Prandoni I., Gruppioni C., Sault R. J., de Zotti G., 2006, A&A, 445, 465

Safouris V., Hunstead R. W., Prouton O. R., 2003, PASA, 20, 1

Saikia D. J., Gupta N., 2003, A&A, 405, 499

Sault R. J., Teuben P. J., Wright M. C. H., 1995, in Shaw R. A., Payne H. E., Hayes J. J. E., eds, ASP Conf. Ser. Vol. 77, Astronomical Data Analysis Software and Systems IV, Astron. Soc. Pac., San Francisco, p. 433

Schlegel D. J., Finkbeiner D. P., Davis M., 1998, ApJ, 500, 525

Shortridge K., 1993, in Hanisch R. J., Brissenden R. J. V., Barnes J., eds, ASP Conf. Ser. Vol. 52, Astronomical Data Analysis Software and Systems II, Astron. Soc. Pac., San Francisco, p. 219

Simpson C., Clements D. L., Rawlings S., Ward M., 1993, MNRAS, 262, 889

Slee O. B., 1977, Aust. J. Phys. Astrn. Supp., 43, 1

Slee O. B., 1995, Aust. J. Phys., 48, 143

Slee O. B., Higgins C. S., 1973, Aust. J. Phys. Astrn. Supp., 27, 1

Slee O. B., Siegman B. C., 1988, MNRAS, 235, 1313

Tadhunter C. N., Dickson R. C., Shaw M. A., 1996, MNRAS, 281, 591

Tadhunter C., Dickson R., Morganti R., Robinson T. G., Wills K., Villar-Martín M., Hughes M., 2002, MNRAS, 330, 977

Tadhunter C., Robinson T. G., González Delgado R. M., Wills K., Morganti R., 2005, MNRAS, 356, 480

Tody D., 1986, in Crawford D., ed., Instrumentation in Astronomy VI. Vol. 627. SPIE, Bellingham, p. 733

Tonry J., Davis M., 1979, AJ, 84, 1511

Wild V., Heckman T., Charlot S., 2010, MNRAS, in press (arXiv:1002.3156)

Wills B. J., 1975, Aust. J. Phys. Astrn. Supp., 38, 1

Wright E. L., 2006, PASP, 118, 1711

Wright A., Otrupcek R., 1990, Parkes Catalog 1990, Australia Telescope National Facility, Sydney

Wright A. E., Wark R. M., Troup E., Otrupcek R., Hunt A., Cooke D. J., 1990, PASA, 8, 261

Wright A. E., Griffith M. R., Burke B. F., Ekers R. D., 1994, ApJS, 91, 111

APPENDIX A: FLUX MEASUREMENTS

In Table A1 we present radio flux measurements of B1221−423 from the literature.

This paper has been typeset from a TeX/LaTeX file prepared by the author.